Intriguing Behavioral Characteristics of Rare-Earth-Free Flux Switching Wind Generators at Small- and Large-Scale Power Levels

Udochukwu B. Akuru, *Member, IEEE*, and Maarten J. Kamper, *Senior Member, IEEE*

***Abstract*—In this study, the design optimization of rare-earth-free flux switching machines (FSMs), viz., ferrite permanent magnets (PMs) and wound-fields (WFs), 12-stator slots/10-rotor poles (12/10) and 12/14, has been undertaken in finite element analyses for wind generator applications, in both small-scale (10 kW) and industrial-scale (3 MW) power levels. The focus is on the performance feasibility of these machines to replace rare-earth PMs, as well as on the suitability of the proposed machines for industrial-scale wind power generation. Hence, it is found that the high torque ripple effects typified by the flux focusing characteristics of FSMs are not enhanced by simply using rare-earth-free materials in place of rare-earth PMs, as is usually suggested. Among other listed findings, it is also found that at 10 kW power, the ferrite PM–FSM performs better in terms of lowest torque ripple and active mass, for both machine configurations. At 3 MW power, WF–FSMs have better torque densities, while ferrite PM–FSMs have better torque ripple values, which result in drastic reductions in the cost of the WF–FSMs at industrial-scale power levels compared to other sampled wind generator topologies. To this end, a 10 kW WF–FSM prototype of the considered variant was manufactured and tested for the first time, with some novel implementations. Based on the reported measured no-load to full-load tests, the study is proven beyond reasonable doubt.**

***Index Terms*—Ferrite permanent magnet (PM), finite element analyses (FEA), flux switching machine (FSM), wind generator, wound-field (WF).**

I. Introduction

THE growth and development of wind energy for power generation in the last few decades has been unprecedented, with wind power dominating the global net renewable power generating capacity over the years [1], while prompting significant interest in the design and manufacturing of wind generators—a major component in wind turbines.

Meanwhile, recent works have focused more on the design and implementation of nonconventional machines for wind power generation [2]–[4]. To this end, flux switching machine (FSM) constitutes a typical nonconventional electrical machine that is being applied for wind power generation due to its high torque density, good voltage regulation, and efficiency as undertaken in [5]. The traditional design of FSMs uses rare-earth permanent magnets (PMs) such as NdFeB or SmCo as overviewed in [6]. However, recent studies [7]–[9] are beginning to focus more on rare-earth-free topologies, such as ferrite PM or wound-field (WF) topologies, due to the following major reasons:

1) PM–FSMs are PM-intensive machines with lowest torque per PM mass ratio compared to the conventional PM machines [8], while adopting so-called flux focusing principles.
2) Rare-earth PMs are highly priced compared to ferrite PMs.
3) The market structure of rare-earth PMs is a monopoly.

As it stands, FSMs are increasingly gaining popularity, not only in design and analyses, but in a wide variety of applications. Among the numerous topologies in existence today and currently under development, it has been shown that the simple radial-flux topology is proven as the most interesting topology [6]–[9], among which are the three-phase 12-stator slots/10-rotor poles (12/10) and 12/14 designs as illustrated in Fig. 1. Already, a number of studies have considered the design and/or analyses of these two machine variants based on PM field excitation sources, [8]–[10] to mention a few. Although ferrite PMs have been routinely used in such studies, but due to their

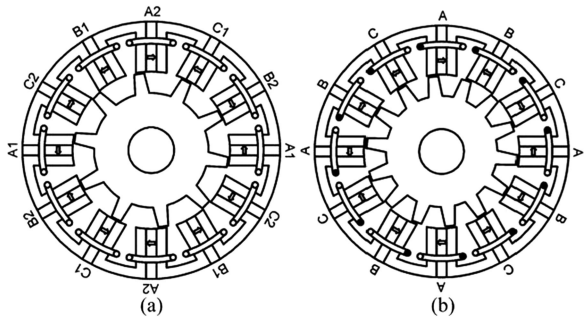

Fig. 1. Cross section of simple radial-flux three-phase PM–FSM topologies. (a) 12/10 machine. (b) 12/14 machine.

Manuscript received January 31, 2018; revised April 27, 2018; accepted June 11, 2018. Date of publication June 18, 2018; date of current version October 12, 2018. Paper 2018-EMC-0171.R1, presented at 2016 IEEE XXII International Conference on Electrical Machines, Lausanne, Switzerland, Sep. 4–7, and approved for publication in the IEEE Transactions on Industry Applications by the Electric Machines Committee of the IEEE Industry Applications Society. This work was supported by the National Research Foundation (NRF) and the Department of Science and Technology (DST) of South Africa. *(Corresponding author: Udochukwu B. Akuru.)*

U. B. Akuru is with the Department of Electrical and Electronic Engineering, Stellenbosch University, Stellenbosch 7600, South Africa, on leave from the Department of Electrical Engineering, University of Nigeria, Nsukka 410001, Nigeria (e-mail: udochukwu.akuru@unn.edu.ng).

M. J. Kamper is with the Department of Electrical and Electronic Engineering, Stellenbosch University, Stellenbosch 7600, South Africa (e-mail: kamper@sun.ac.za).

Color versions of one or more of the figures in this paper are available online at http://ieeexplore.ieee.org.

Digital Object Identifier 10.1109/TIA.2018.2848979

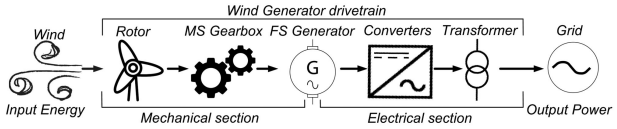

Fig. 2. Proposed geared MS FS wind generator drivetrain.

low energy potentials, they are not so much popular like those designed with rare-earth PMs.

As for the WF designs, the 12/10 and 12/14 topologies shown in Fig. 1 were first conceptualized in [11], with comparable torque capabilities to similar PM–FSM designs exhibited. However, eventually, only the 12/14 WF–FSM was analyzed in finite element analyses (FEA) without any design optimization or experimental measurement reported, while the 12/10 topology was entirely abandoned. Ever since then, no other study, in the authors' best knowledge, has considered these WF–FSM topologies.

Much later, consideration on the preferred 12/10 WF–FSM topology was intensified in [7] and [12]. While the current study is meant to be a follow-up of the study in [7] where the focus was primarily on 12/10 rare-earth-free machines at 1.5 kW power, it should be noted that the study in [12] was strictly on the formulation of a multiobjective design optimization (MDO) approach and how it influences the manufacturing and performance indices of WF–FSMs, based only on the 12/10 topology at 10 kW power. In this study, both the 12/10 and 12/14 (refer to the Appendix for the speed and frequency range of both machines) WF–FSM and ferrite PM–FSM topologies are designed, optimized, and characterized for small-scale (10 kW) and large-scale (3 MW) wind generator applications. Toward the end, one of the 10 kW 12/10 WF–FSM optimal design candidates is nominated and experimented.

As indicated, the main motivation for this study is to expose the potentials of these machine topologies for wind power generation as being done in transportation and aerospace systems [8]–[10], [13]. Hence, because it is desired for wind generator designs, like in most electrical machine systems, for the cost of the total setup to be minimized as much as possible, one way by which this can be conquered is to use easily accessible and less expensive raw materials like WFs or ferrite PMs for the excitation scheme. Besides, it remains to be seen the behavioral tradeoffs of these rare-earth-free FSMs upon dramatic adjustments of their power range in a robust MDO environment. Therefore, with the right power range, a proper account on the effects of scaling the proposed wind generators can be made available, especially to provide insights for wind generator designers and manufacturers.

The optimum design characterization of both the 12/10 and 12/14 machines, implemented as rare-earth-free configurations, would be undertaken in two-dimensional (2-D) static FEA, for small-scale (10 kW) and large-scale (3 MW) wind generator drives. The wind generator is proposed for the geared medium-speed (MS) drivetrain illustrated in Fig. 2, which has been declared as the best in terms of performance to cost index for different generator topologies [14]. The focus of the study, however, is mainly on the electromagnetic design and analyses of the wind generator itself in respect to other drivetrain components.

In the subsequent sections, a description of the design optimization method used for the study is briefly recounted, after which the optimization results are discussed for the designated power levels. Thereafter, some selected optimal design samples are compared *ab intra* and *inter alios* to other conventional wind generator topologies analyzed in the literature, within the same drivetrain. The penultimate section is dedicated toward comparing the 2-D FEA results with corresponding 3-D FEA evaluations of some benchmark designs, especially toward highlighting the impacts of 3-D end effects in the 3 MW machines, after which the last section is used to report the experimental evaluation of a selected optimal 10 kW WF–FSM benchmark.

II. Design Optimization Process

It is commonly agreed that in the design optimization of electrical machines, a constrained multiobjective problem is the preferred choice, due to many conflicting design parameters competing for relevance [15]. However, the contention is still on the preferred optimization algorithm—be it deterministic or stochastic (metaheuristic). Whereas the former is fast, cheap, and follows the gradient method, it is limited because it depends on a predefined starting point which may lead the optimal solution astray in the event that many local minima/maxima exist inside the search arena. Instead, stochastic algorithms which are inauspiciously time and cost intensive are more flexible and attractive to tackle global optimization problems. Although there is equally no guarantee that a firm optimal solution can be obtained with such metaheuristics because of their nongradient solutions, however, there is a high chance that the final solution lies very, very close.

Thus, the Nondominated Sorting Genetic Algorithm II (NSGA–II) is a typically robust metaheuristic [16], which has been basically adopted in this paper. A major highpoint in the use of NSGA–II for electrical machine design optimization is the fact that it can generate a Pareto optimal solution set when invited to multiobjective problems as previously propagated in [17] to brushless doubly fed induction machines.

To this end, NSGA–II linked by FEA evaluations is being escalated further in the design analyses of the proposed rare-earth-free FSMs, based on a constrained MDO approach. Besides, the optimization suite [18], where the NSGA–II functionality is readily accessible, is used alongside a robust and versatile 2-D static FEA open-source package—SEMFEM [19]. Both simulation tools are interfaced as shown in Fig. 3. The 2-D FEA workflow shows how each model is conceived and solved in SEMFEM, and then tossed back-and-forth through the VisualDOC optimizer until some convergence is obtained.

The optimization problem to be tackled, which requires the minimization of two objectives and the declaration of three design constraints, is set up as follows:

$$F(\bar{x}) = \begin{bmatrix} M_A \\ \kappa_\delta \end{bmatrix}; G(\bar{x}) = \begin{bmatrix} pF \\ P_{\text{out}} \\ \eta \end{bmatrix} \tag{1}$$

$$\bar{x} = \begin{bmatrix} \alpha & g & J & J_F & l_{\text{st}} & D_{\text{out}} & D_{\text{in}} & D_{\text{sh}} & b_{\text{pm}} & b_F & b_{\text{pr}} & b_{\text{sls}} & h_{\text{ys}} & h_F & h_{\text{yr}} & t_0 \end{bmatrix} \tag{2}$$

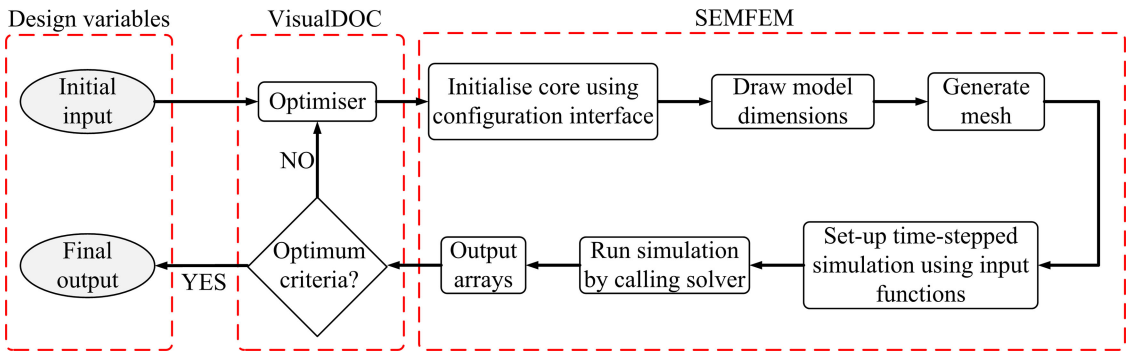

Fig. 3. FEA design optimization procession.

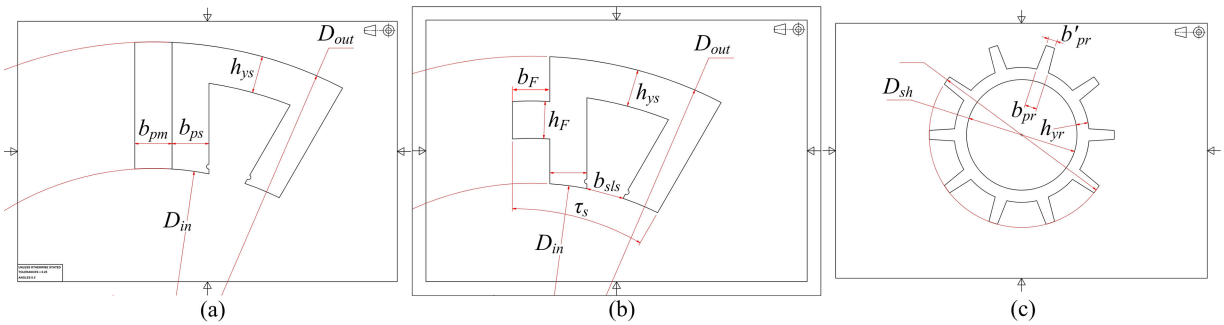

Fig. 4. Highlights of key dimensional parameters as conceived. (a) PM–FSM stator lamination. (b) WF–FSM stator lamination. (c) Rotor lamination.

with M_A representing the total active mass, κ_δ is the peak-to-peak torque ripple, P_{out} is the output power, η is efficiency, and pF is power factor. The selection of these parameters is incumbent on the following.

1) Minimum mass: The total component mass of a wind generator plays a significant role in determining not only the size, but also the costs of the general wind turbine assembly. Therefore, minimizing the generator mass is bound to increase the power density at lower the drivetrain manufacturing and installation costs.
2) Minimum torque ripple: A low torque ripple is critical for the survival of the drivetrain, whereby it constitutes mechanical stress. Thus, because FSMs are generally known to suffer from high torque ripple values, the objective target is meant to address this problem.
3) Maximum efficiency and power factor: A high efficiency is important to improve the cost-energy ratio of not only the wind generator, but also the overall system, while a high power factor is required to minimize the size and cost of the inverters.

Based on the 2-D FEA process, the end-windings have been modeled accordingly as described already in [12]. Also, formulations of the active mass, torque ripple, output power, efficiency, and power factor used in the optimization process are as indicated in [12]. A total of 12 and 13 design parameters ($\bar{x}$) are varied for the ferrite PM–FSM at 10 kW and 3 MW, respectively. On the other hand, 14 design variables are registered for the WF–FSM at both 10 kW and 3 MW power levels. The total design variables summoned at any time for the optimization procedure is comprised in the array expression in (2), where g is the airgap length, J is the armature current density, J_F is the field current density only for the WF–FSM design, l_{st} is the stack length, D_{out} is the stator outer diameter, D_{in} is the stator interior diameter, D_{sh} is the rotor shaft diameter, b_{pm} is the PM length only for the ferrite PM–FSM, b_F is the field iron core length only for the WF–FSM, b_{pr} is the rotor pole width, b_{sls} is the stator slot opening width, h_{ys} is the stator yoke height, h_F is the field iron core width only for the WF–FSM, h_{yr} is the rotor yoke height, and t_0 is a tapering factor for the rotor teeth. The current angle α is defined as

$$\alpha = \tan^{-1}\left(I_q / I_d\right) \tag{3}$$

where I_q and I_d are the d- and q-axes currents of the phase current, respectively. A visual representation of key dimensional variables is attempted as shown in Fig. 4, for both the PM–FSM and WF–FSM topologies.

Due to the high sensitivity of the WF–FSM designs to copper loss which limits the efficiency requirements, their copper windings were estimated at operating temperatures of 80 °C in order to increase the design reliability, but that of the ferrite PM–FSMs were retained at room temperature values (25 °C). In addition, the efficiency and output power specifications are administered differently depending on either the power level or the type of field source used. For instance, the power limits for all the kW designs was registered to at least 10 kW, while that of the MW designs to at least 3 MW. The efficiency of all 3 MW designs was specified to at least 97%, while those of the 10 kW ferrite PM–FSMs and WF–FSMs were settled at "least" minimums of 90% and 89%, respectively.

In NSGA–II, the primary fitness is evaluated based on domination level while the secondary fitness is evaluated based on the diversity of the solution in its domination level, each fitness level

TABLE I
NSGA-II PARAMETERS

Parameters	Ferrite PM–FSM		WF–FSM	
	10 kW	3 MW	10 kW	3 MW
Mutation probability	0.083	0.076	0.071	0.071
Crossover probability	0.9	0.9	0.9	0.9
Mutation distribution index	10	10	10	10
Crossover distribution index	20	20	20	20
Population size	20	25	20	20
Iterations	100	100	100	100

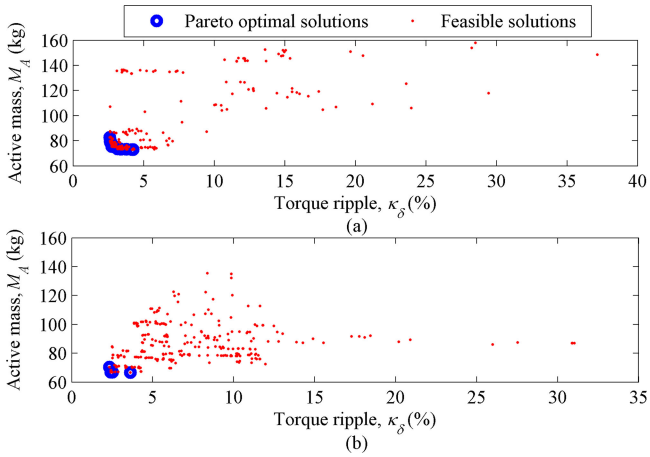

Fig. 5. Pareto optimal fronts for different 10 kW ferrite PM–FSMs. (a) 12/10. (b) 12/14.

represented as user-tunable parameters. Further descriptions on these parameters are elucidated in [16]. Thus, for the different simulations undertaken in this study, it was necessary to tune the NSGA–II operators as indicated in Table I. The difference observed in the mutation probability is because it is taken as the inverse of the number of design variables considered for each MDO problem category indicated. For each problem, the upper and lower boundaries of the prescribed design parameters are also fine-tuned to ensure geometrical feasibility. The results obtained after each simulation are presented and discussed in the subsequent section.

III. Design Optimization Results and Discussions

The optimization results for the 12/10 and 12/14 machines at 10 kW and 3 MW are displayed in Figs. 5–8. At 10 kW power, the optimal candidates of the 12/14 ferrite PM–FSM yield a slightly smaller active mass and lower torque ripple values compared to optimal candidates of the 12/10 ferrite PM–FSM, as shown in Fig. 5. In Fig. 7, a similar outcome is represented for the ferrite machines at 3 MW power levels, whereby decrease in active mass is more significantly represented in the 12/14 optimal candidates compared to the 12/10 optimal designs.

On the other hand, Fig. 6 indicates that the 10 kW WF–FSM optimal designs are not able to produce lower torque ripple values usually expected of the 12/14 machines when compared to their 12/10 counterparts. Rather, it is observed that the 12/10 machines achieve lower torque ripples much beyond the values realizable in the 12/14 machines, but at a slightly bigger active

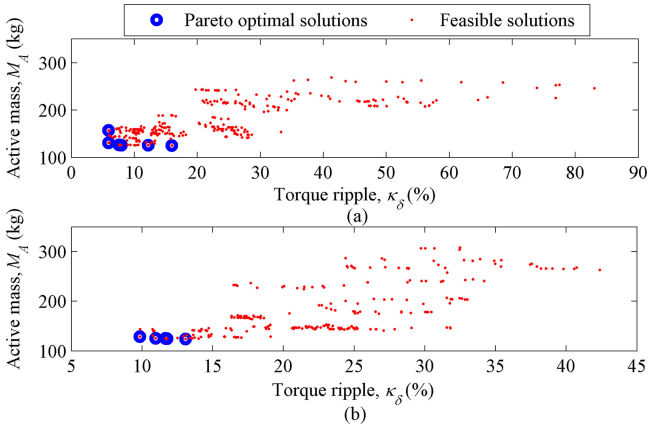

Fig. 6. Pareto optimal fronts for different 10 kW WF–FSMs. (a) 12/10. (b) 12/14.

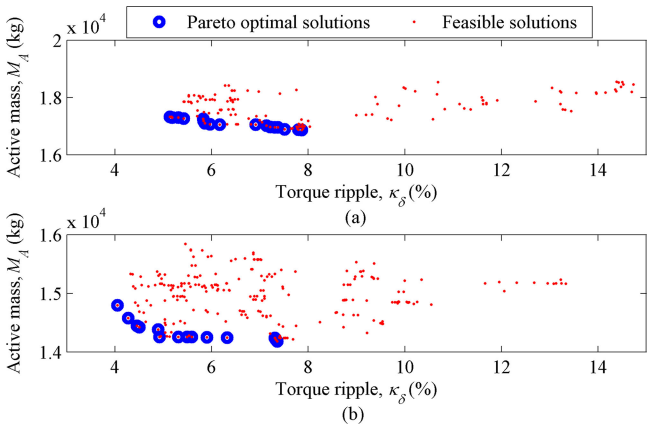

Fig. 7. Pareto optimal fronts for different 3 MW ferrite PM–FSMs. (a) 12/10. (b) 12/14.

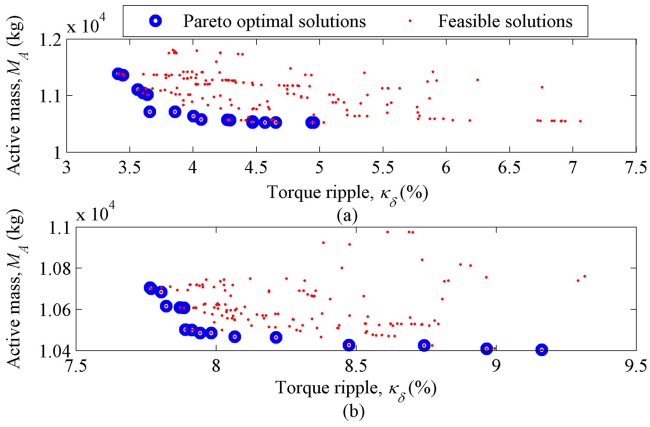

Fig. 8. Pareto optimal fronts for different 3 MW WF–FSMs. (a) 12/10. (b) 12/14.

mass. As observed in Fig. 8, this tendency is further escalated to more than 55% deficit of the lowest torque ripple feasible in the 12/10 machines compared to the 12/14 machines at 3 MW power levels. This discrepancy is due to the efficiency requirements in the WF–FSM, which is inherently limited by the presence of the WF coils, and further suppressed by the higher core losses of the 12/14 machines in relation to the 12/10 machines.

TABLE II
PERFORMANCE COMPARISON OF DIFFERENT MACHINE CHARACTERISTICS FOR GEARED MS WIND GENERATORS

	Design	P_{out} (kW)	τ_e (Nm)	κ_δ (%)	M_{FeS} (kg)	M_{FeR} (kg)	$M_{PM/F}$ (kg)	M_{Cu} (kg)	M_A (kg)	η (%)	pF –	τ_e/V_A (kNm/m^3)	Cost[a] ($US)
Ferrite PM–FSM	12/10	10.017	259.563	3.384	34.164	20.540	11.201	7.576	73.481	94.927	0.805	17.311	317.210
	12/14	10.067	260.988	2.432	28.096	22.474	9.114	7.266	66.951	96.186	0.811	18.701	283.773
	12/10	3063.398	79246.694	5.153	9155.799	4023.046	2531.542	1617.292	17327.681	99.111	0.805	19.953	72422.549
	12/14	3011.434	78044. 441	4.363	7253.789	4378.919	2040.463	1124.986	14798.159	99.018	0.810	22.197	58596.431
WF–FSM	12/10	9.995	249.469	5.877	67.352	42.648	8.854	11.999	130.856	89.090	0.826	8.639	475.553
	12/14	11.371	295.537	9.957	62.005	42.978	9.851	14.086	128.921	89.296	0.790	10.309	499.057
	12/10	2998.164	77841.826	3.736	6575.027	2913.221	685.939	1040.134	11214.322	97.017	0.804	31.586	40206.163
	12/14	3075.991	79616.178	8.733	5660.582	3474.238	587.632	877.086	10599.540	97.429	0.799	34.354	36501.445
A[b]	12/10	3018.262	78354.538	1.344	2363.538	1751.821	619.729	314.650	5049.740	98.875	0.823	58.917	49761.609
	12/14	3044.434	78908.753	1.283	3081.062	1573.498	697.132	535.802	5887.495	99.103	0.832	57.088	58068.930
B[c]	PMSG	3000.000	318309.886	–	4370.000		410.000	1330.000	6110.000	98.000	–	78.179	49110.000
	DFIG	3000.000	318309.886	–	8650.000		2720.000		11370.000	97.000	–	52.119	49494.000

[a]The cost estimations are performed based on quotations in US dollars (USD) mined from [8].
[b]Rare–earth PM–FSM benchmarks imported from [20].
[c]Selected conventional wind generator topologies from [21].
τ_e = average electromagnetic torque, M_{FeS} = stator iron mass, M_{FeR} = rotor iron mass, $M_{PM/F}$ = PM or wound–field mass, M_{Cu} = copper mass of phase windings, V_A = active stack volume, $US = US Dollars.

TABLE III
COMPARISON OF SOME BASIC OPTIMAL DESIGN PARAMETERS

	Design	l_{st} mm	D_{in} mm	D_{out} mm	Λ_0 %	κ_L %	J A/mm^2	J_F A/mm^2	g mm	n_r r/min
Ferrite PM–FSM	12/10	139.415	234.875	370.043	63.472	59.357	4.607	–	0.700	360
	12/14	144.888	235.033	350.201	67.113	61.645	3.824	–	0.700	360
	12/10	1311.451	1318.522	1963.627	67.147	99.463	1.079	–	2.756	360
	12/14	1316.814	1325.971	1843.780	71.915	99.309	1.228	–	2.624	360
WF–FSM	12/10	97.135	435.244	615.212	70.746	22.317	1.434	4.958	0.700	360
	12/14	97.650	429.558	611.380	70.260	22.732	1.224	4.918	0.700	360
	12/10	507.185	1695.249	2487.295	68.156	29.918	1.004	4.999	3.000	360
	12/14	540.303	1668.408	2336.922	71.393	32.384	1.014	4.994	3.000	360
A	12/10	702.434	1234.381	1552.608	79.503	56.905	4.975	–	2.514	360
	12/14	693.796	1152.776	1592.681	72.379	60.184	2.087	–	2.995	360
B	PMSG	400.000	–	3600.000	–	–	–	–	3.600	90
	DFIG	600.000	–	3600.000	–	–	–	–	2.000	90

$\Lambda_0 = D_{in}/D_{out}$ (split ratio), $\kappa_L = l_{st}/D_{out}$ (aspect ratio), n_r = mechanical speed in r/min.

Considering the 10 kW machines (Figs. 5 and 6), it is noteworthy to see that the best optimum designs (lowest torque ripple and smallest active mass) were obtained for the 12/10 and 12/14 ferrite PM–FSMs. However, the same cannot be said for the 3 MW designs (Figs. 7 and 8), whereby the active mass is generally smaller for both the 12/10 and 12/14 WF–FSMs, but with lower torque ripple obtained in the 12/10 WF–FSM and 12/14 ferrite PM–FSMs. Essentially, a better mass minimization occurs in the WF–FSMs compared to the ferrite PM–FSMs at 3 MW power levels by up to 34% and 28%, for the 12/10 and 12/14 machines, respectively. This is a very crucial find, especially given that the copper windings in the WF–FSMs were modeled to the feasible temperature of 80 °C, unlike for the ferrite PM–FSMs which were kept at room temperature condition.

To discover the reason for the significant active mass minimization of the WF–FSM compared to ferrite PM–FSMs at 3 MW power levels, eight designs are initially benchmarked from each of the obtained optimal solution sets and compared as shown in Tables II and III. Based on the values reported, one can observe that the discrepancy in mass, between the optimal ferrite PM–FSM and WF–FSM designs at 3 MW power levels, is influenced by interactions between the armature current density and aspect ratio. In response to the set design optimization targets, it is noticed that the aspect ratios of the ferrite PM–FSMs at 3 MW power increased drastically, whereas its current densities decreased in tandem, when compared to the 10 kW machines. However, the same cannot be said for the 3 MW WF–FSMs, whereby it is observed that similar values are maintained when both parameters are compared accordingly. Thus, based on the set of complete design points operated during the MDO process, both feasible and infeasible, a linear relationship between the armature (phase) current density and aspect ratio has been correlated for the 3 MW rare-earth-free machines as shown in Fig. 9, which confirms their optimal behavior in the liberal MDO design space. Note that, the active optimal solutions of the 3 MW ferrite PM–FSMs and WF–FSMs are mainly situated in the region of current density values of 1—1.5 A/mm^2, as shown in Fig. 9.

Generally, Table II also reveals that the 12/14 machines result in higher torque per active stack volumes compared to the 12/10 machines, irrespective of the type of rare-earth-free excitation or operating power level. Some 3 MW rare-earth PM–FSMs imported from [20], presents an exception to the case, whereby a very sharp difference indicated for their armature current densities is implicated as the main culprit.

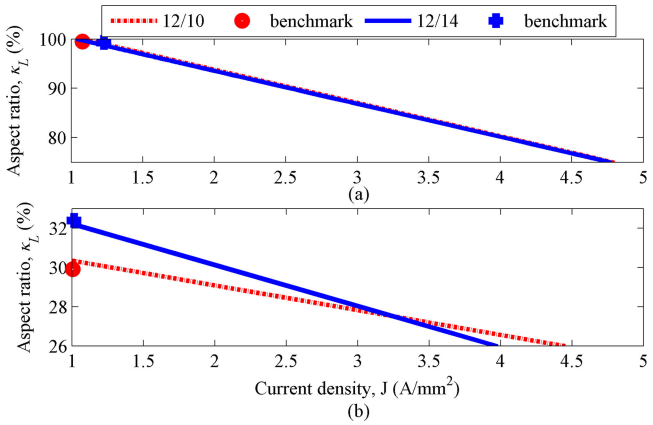

Fig. 9. Optimal partnership between current density and aspect ratio in 3 MW rare-earth-free FSMs. (a) Ferrite PM–FSM. (b) WF–FSM.

TABLE IV
PER-UNITIZED REACTANCES AND INDUCTANCE RATIO

	Excitation	α (deg.)	I_s (A)	X_d (pu)	X_q (pu)	X_s (pu)
12/10 10 kW	Rare–earth[a]	70.795	11.673	0.848	0.475	0.661
	Ferrite	68.732	11.651	0.697	0.510	0.603
	Wound–field	80.809	8.243	0.855	0.392	0.623
12/14 10 kW	Rare–earth[a]	30.322	11.466	0.648	0.790	0.719
	Ferrite	44.633	8.924	0.397	0.566	0.481
	Wound–field	48.644	8.217	0.423	0.534	0.478
12/10 3 MW	Rare–earth[a]	64.061	103.714	1.075	0.542	0.808
	Ferrite	74.202	61.935	0.718	0.459	0.947
	Wound–field	70.010	95.838	1.397	0.497	0.947
12/14 3 MW	Rare–earth[a]	40.607	75.020	0.593	0.612	0.602
	Ferrite	49.120	48.840	0.379	0.518	0.448
	Wound–field	41.070	76.651	0.784	0.613	0.698

[a]Rare–earth PM–FSM benchmarks imported from [20].
I_s = RMS phase current, X_d = d–axis reactance, X_q = q–axis reactance, X_s = synchronous reactance.

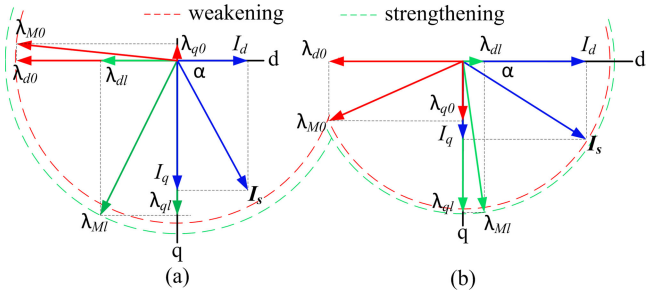

Fig. 10. Generalized magnetic field behavior of space phasor diagrams for the different optimal FSMs. (a) 12/10 machine. (b) 12/14 machine. λ_{d0}, λ_{q0} = d- and q-axes flux linkage at no-load, λ_{dl}, λ_{ql} = d- and q-axes flux linkage at full-load, λ_{M0}, λ_{Ml} = net armature-reaction flux linkage at no-load and full-load, I_d, I_q = d- and q-axes currents, $\boldsymbol{I}_s$ = peak phase current.

In terms of total cost of active materials, the 12/14 rare-earth-free machines are thus cheaper compared to their 12/10 machines as indicated. Again, the exception to the case (the 10 kW 12/14 WF–FSM benchmark) is due to the output power exceeding the optimal 10 kW design threshold. On the other hand, comparing the ferrite PM–FSM and WF–FSM shows that the cost of the latter is higher for the 10 kW machines and lower for the 3 MW machines due to tradeoffs observed in their total active mass at the different power levels.

The latter rows in Tables II and III are provided to highlight the comparative performance characteristics of the rare-earth-free FSM design candidates at 3 MW power levels only in relation to the rare-earth PM–FSMs considered in [20], as well as other traditional geared MS wind generators sourced from the literature, viz., permanent magnet synchronous generator (PMSG) and doubly-fed induction generator (DFIG). Information on the key data for the PMSG and DFIG machines were retrieved from the study in [21]. With this additional information, it is clearly shown that the cheapest generator active material cost at 3 MW power is expressed by the WF–FSM, compared to the rest. Notwithstanding, the PMSG, rare-earth PM–FSM, and DFIG systems produce significant torque densities compared to the WF–FSM. This is because the PMSG and DFIG are designed at lower rated speed and perhaps due to their large split and small aspect ratios as indicated by the stator outer diameters and stack lengths shown in Table III. Whereas, it should also be noted that the rare-earth PM–FSM, in addition to the PMSG, are both designed using high-energy quality rare-earth PMs. Yet, it must be reiterated that the main interest in this study is to despise the use of more expensive rare-earth PMs such as the PMSG and the rare-earth PM–FSM, while on the other hand, for certain DFIGs, the generator maintenance costs are exacerbated due to their usage of slip rings and brushes.

Meanwhile, observe that the concentration of the optimum design solutions of the ferrite PM–FSM on lower armature current densities and higher split ratios resulted in them being the most expensive designs at 3 MW power levels. Based on the NSGA–II optimization algorithm used in this study, the unlikely situation obtained for the ferrite PM–FSM at industrial-scale power levels could be resolved if only the margin of the aspect ratio is set to smaller values (75–85%) while alternatively increasing the margin of the split ratio before the MDO process is placed on the spot.

Also, it is equally observed from Table II that the 3 MW machine credited with the highest cost of generator active material and lowest torque density, viz., the ferrite PM–FSM, yields the best generator efficiency at over 99%, with the rare-earth PM–FSM following closely. But because the copper resistivity used in the design process of the ferrite and rare-earth PM–FSMs were approximated at much lower temperature coefficients than for the WF–FSM, the purported achievement of high efficiency is therefore not conclusive. But, it should be noted that the presence of the WF coils in the WF–FSM designs introduce additional burden on the efficiency requirements.

Meanwhile, there appears to be a general misconception on how much the flux focusing characteristics influence the torque ripple in FSMs. Such claims have been made in [22], which appears to have been discredited in the resolved MDO scenario as it appears in Table II, where the use of rare-earth-free materials have not resulted in lower torque ripple values.

In Table IV, the synchronous per unit reactance of the FSM benchmarks at different power ratings are compared. It is clearly observed that similar range of low values is evinced, irrespective of the power level or whether the excitation is designed with rare-earth or rare-earth-free materials. According to Boldea *et al.* [4], such low reactance values (less than 1 p.u.) are economically advantageous to the power converters. On the

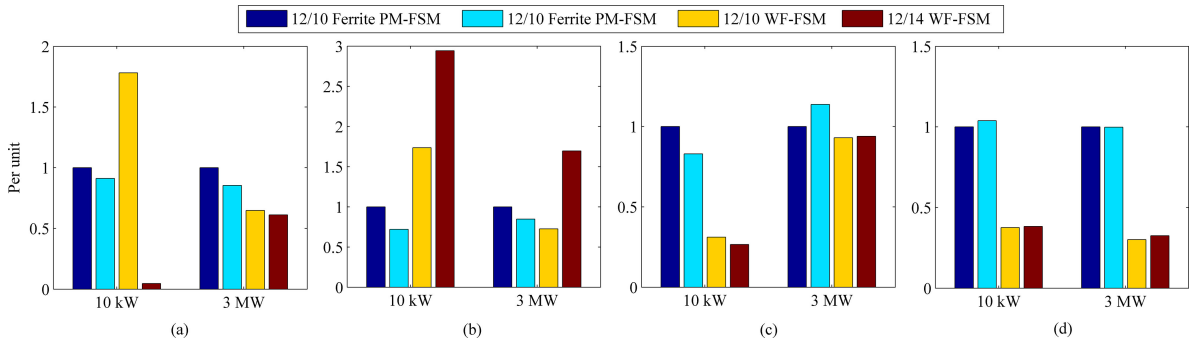

Fig. 11. General highlights of the studied rare-earth-free FSMs compared in per unit in terms of: (a) total active mass, (b) torque ripple, (c) phase current density, and (d) aspect ratio (base values are taken on the 12/10 ferrite PM–FSM for each compared item).

TABLE V
COMPARATIVE PERFORMANCE CHARACTERISTICS OF 3 MW WF–FSM BENCHMARKS IN 2-D AND 3-D FEA

Design	τ_e (kNm)		P_{Cu} (kW)		κ_δ (%)	
	2–D	3–D	2–D	3–D	2–D	3–D
12/10	77.841	72.949	68.513	67.299	3.736	23.166
12/14	79.616	71.617	52.951	52.561	8.733	16.923

other hand, high inductance ratios ($X_d : X_q$) are mostly observed in the 12/10 machines as against that of the 12/14 machines due to disparities in their optimum current angles (α) shown in Fig. 10. It is further observed in Fig. 10 that, under load, a complex d–q axes magnetic interchange erupts in both machines such that the d-axis no-load flux (λ_{d0}) is weakened, whereas that of the q-axis (λ_{q0}) becomes strengthened.

In summary, the relative characteristics of the 12/10 and 12/14 rare-earth-free FSMs are quantitatively compared at 10 kW and 3 MW power levels, in terms of some of the key design issues studied, as shown in Fig. 11. Thus, the preferred solution for the proposed rare-earth-free wind turbine generator, especially at industrial scale, is nominated from the 3 MW WF–FSM design candidates. Hence, to partially substantiate the 2-D static FEA evaluations, the two 3 MW WF–FSM benchmarks are propagated in 3-D transient FEA evaluation as discussed in the ensuing section.

IV. 3-D FEA EVALUATIONS

As easily understood, the overlapping of the phase coils over the WF coils may portray significant effects in the end-windings of WF–FSMs compared to ferrite PM–FSMs. Besides, it should be noted that the current study has been used to report the performance of these machines at industrial-scale power levels, which makes it even more important to establish the accuracy of the 2-D static FEA predictions by performing additional 3-D FEA evaluations. The 3-D FEA is based on transient simulations exercised using the commercial ANSYS Maxwell software. To this end, the two 3 MW WF–FSMs benchmarks in the preceding section have been nominated for the procedure.

The magnetic field distributions of the models in 2-D FEA, as well as their magnetic flux density map in 3-D FEA, are both displayed as shown in Fig. 12. Without doubt, the end-leakages are highly dominant in the 3-D models as seen on all its sides,

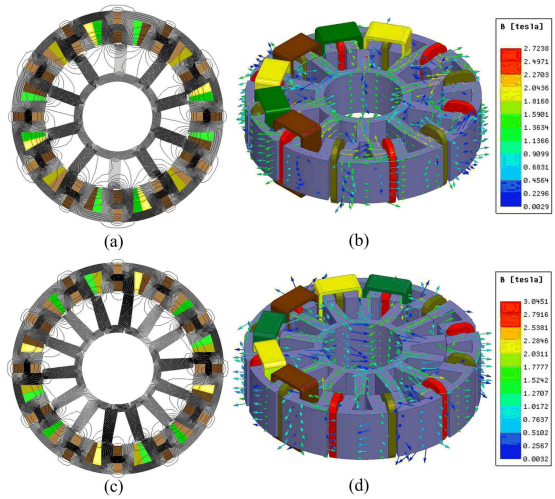

Fig. 12. Magnetic flux distributions and flux densities at rated load condition for the different 3 MW WF–FSMs. (a) 12/10 in 2-D. (b) 12/10 in 3-D. (c) 12/14 in 2-D. (d) 12/14 in 3-D.

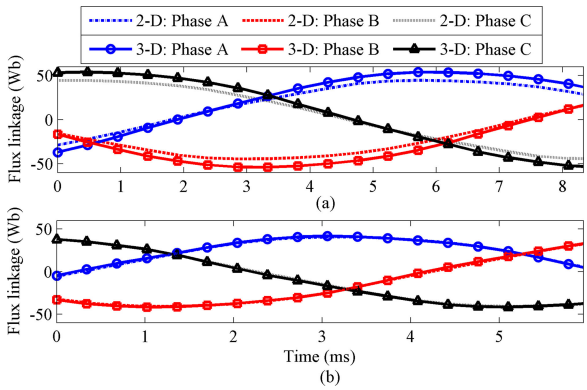

Fig. 13. On-load phase flux linkage waveforms plotted over half electrical period for the different 3 MW WF–FSMs. (a) 12/10. (b) 12/14.

including the surfaces defined at both ends of the axial path, as well as inside the rotor shaft boundaries, compared to the 2-D models. As a result, a decrease in the torque capability in the 3-D models as later compared in Table V is acceptable at face value.

The on-load phase flux linkages evaluated in 2-D and 3-D FEA are compared as shown in Fig. 13. The 12/14 machine displayed good confidence with 2.2% discrepancy between both

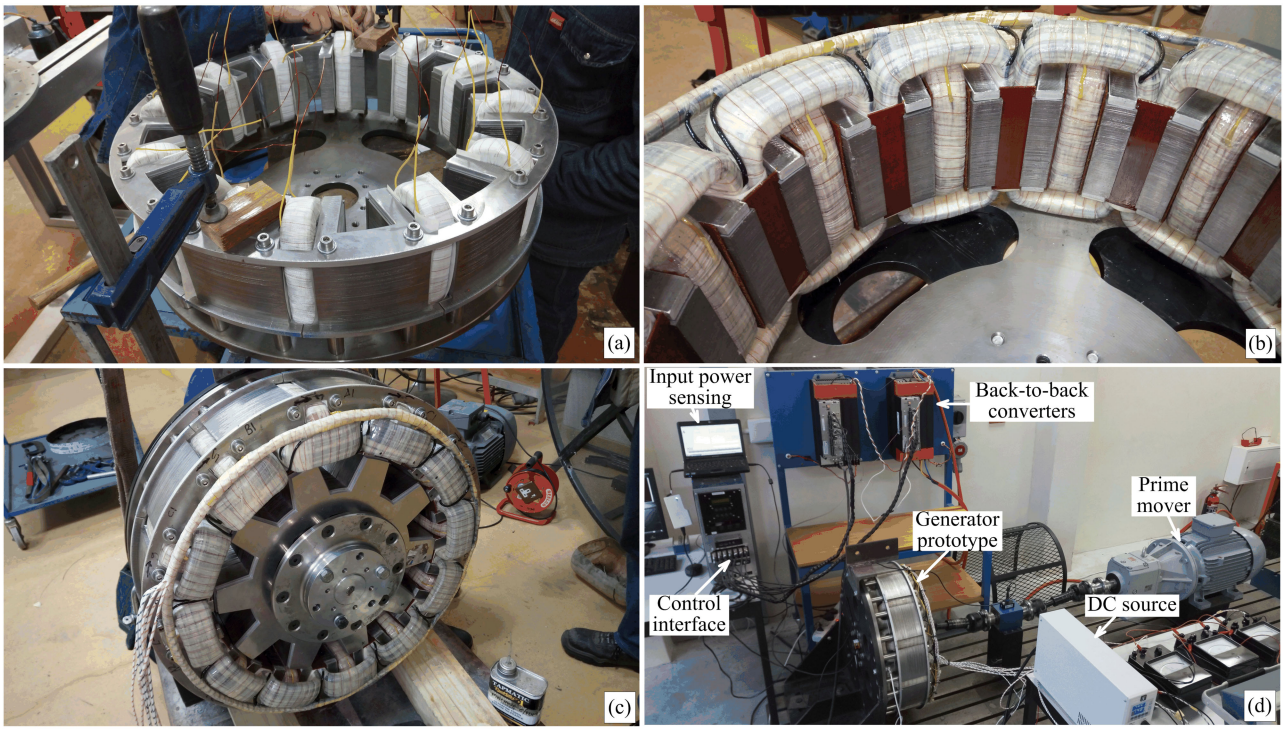

Fig. 14. Prototype development and testing of 10 kW WF–FSM. (a) Manufacturing parts. (b) Varnished coils. (c) Assembled machine. (d) Experimental rig.

techniques. However, a higher discrepancy (17.5%) is observed in the 12/10 machine due to underestimation of the imposed clearances of the phase end-winding in the end sections of the lamination stack in 2-D FEA.

Table V shows the average electromagnetic torque, torque ripple, and total copper loss readings evaluated in both 2-D and 3-D FEA. As earlier insinuated, the differences observed in the torque values due to end-leakage effects observed in the 3-D designs compared to 2-D, despite differences in the mesh densities applied in 2-D (finer) as opposed to 3-D (coarser), is the primary culprit for the torque ripple discrepancies.

V. Experimental Verification

In this section, the experimental validation of one of the rare-earth-free FSM wind generator variants proposed in this study has been exercised with a 10 kW WF–FSM optimal design, escalated from the MDO process reported in Section III. The choice of the WF–FSM over the ferrite PM–FSM is due to its comparative excellent performance at 3 MW as shown in Tables II and III, especially when compared to other conventional geared MS wind generators. Moreover, the associated characteristic concerns of PM topologies such as high demagnetization risks due to overheating of the PMs and their prohibitive cost implications are none issues regarding this preference. Unlike in classical WF machines, the studied WF–FSM topology also exhibits a brushless status, with an ease for both voltage regulation and thermal management.

Various stages describing the 10 kW WF–FSM prototype development and testing have been photographically captured, as shown in Fig. 14. The major highlight of the manufacturing process is the implementation of novel segmentations of the stator laminations as typical in its counterpart PM–FSM variant, thereby facilitating the preformation of both the phase and field coils, among others. The preformed field coils were first inserted into each of the resulting 12 stacked stator segments, followed by their assembly on the circular stator end plates [see Fig. 14(a)], and finally, the mounting of the preformed phase coils [see Fig. 14(b)]. Due to the absence of PMs, eccentricity issues with the stator assembly do not suffice [see Fig. 14(c)].

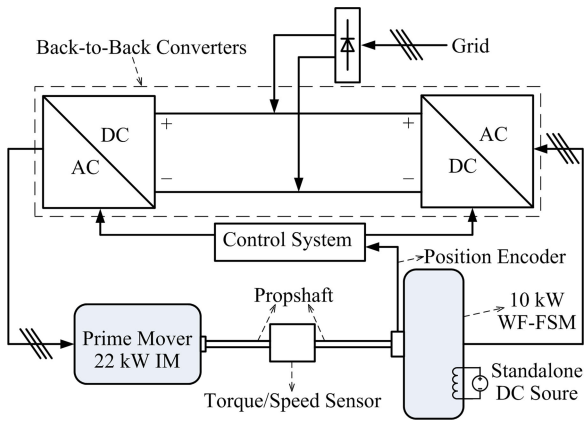

Fig. 15. Laboratory setup of the 10 kW WF–FSM wind generator drive.

A layout of the laboratory test rig for the full current vector controlled 10 kW generator prototype is illustrated in Fig. 15, while Fig. 16 shows the rotor positional and pulsewidth modulated reference voltage signals superimposed onto the lagging steady-state rated current waveform in the generator mode. In Fig. 17, the FEA-predicted torque and phase voltage are compared to measured results from no-load to full-load (9.8 A),

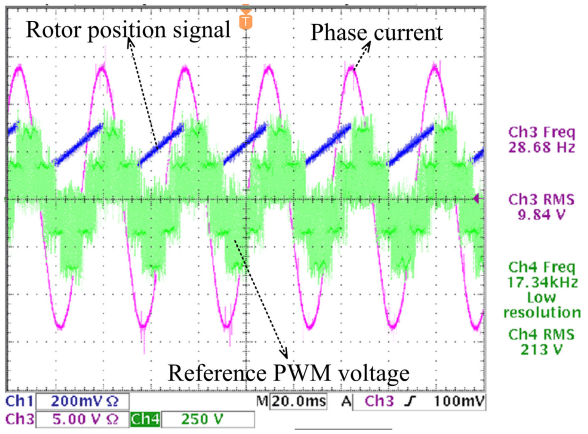

Fig. 16. Measured generator steady-state rated signals at ≈ 180 r/min.

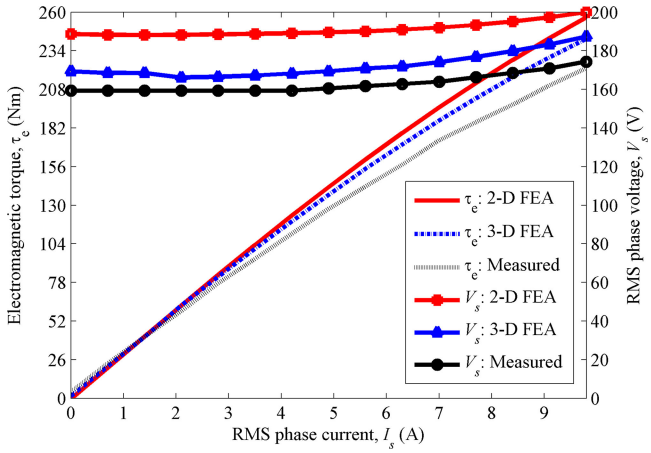

Fig. 17. Characteristics of the generator electromagnetic torque and phase voltage against load current at rated field current and ≈ 180 r/min.

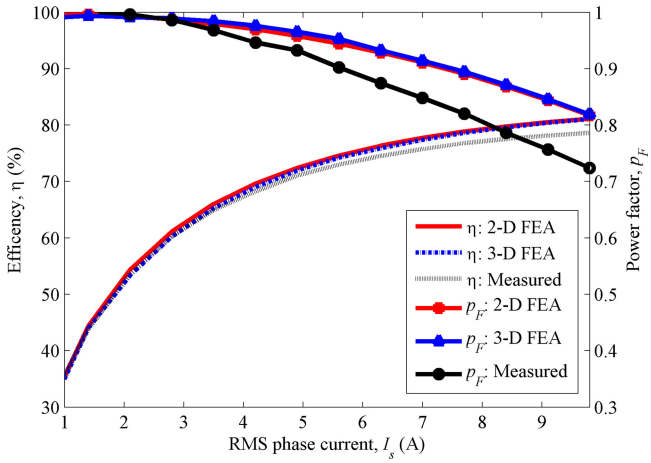

Fig. 18. Characteristics of generator efficiency and power factor versus load current at rated field current and ≈ 180 r/min.

with a good confidence. The efficiency and power factor is also compared as shown in Fig. 18, with a breakdown of the different losses illustrated in Fig. 19. Some of the calculations invoked during the measurements are articulated in the Appendix. Due to 500 V (line voltage) operating limitation of the power converters, the measurements were conducted at half the prescribed

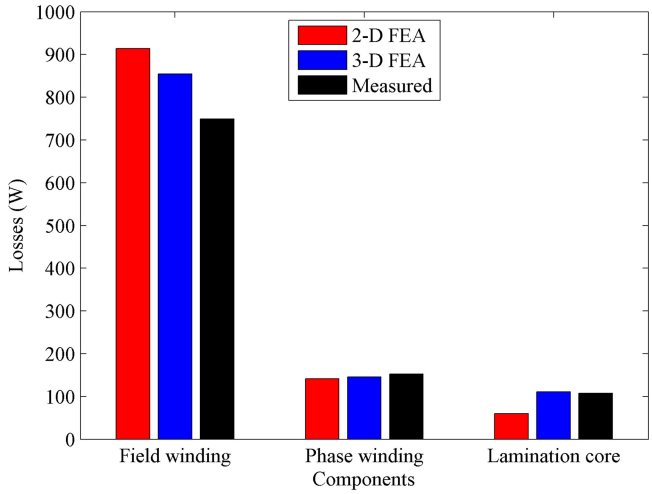

Fig. 19. Breakdown of generator losses at ≈ 180 r/min.

TABLE VI
COMPARISON OF WINDING RESISTANCE

Resistance	2–D	3–D	Lab.
Phase winding (Ω)	0.47	0.49	0.53
Field winding (Ω)	4.18	3.51	3.08

rated speed and with parallel circuits implemented for the field and phase coils, although this does not impact the rated electromagnetic torque requirement. In Fig. 17, the slight increase in generator terminal voltage with increasing load is due to the complex cross magnetization in the space vector *d*- and *q*-axes flux linkages earlier portrayed in Fig. 10. The discrepancies between FEA calculations and measurement, in terms of voltage, torque, and power factor, especially at higher load current, are due to ignored saturation effects and fringe leakages in the FEA models, as well as unmitigated manufacturing errors.

Meanwhile, the deviations observed between the pre-estimated and measured core losses shown in Fig. 19 are mainly due to apparent overestimation of the end-winding coil resistance, especially for the field winding coils compared in Table VI. Despite a few manufacturing infractions incurred during the fabrication of the 10 kW wind generator prototype, the practical measurements, were in general, mentored according to the FEA-measured data.

VI. CONCLUSION

In this paper, two candidate FSMs (12/10 and 12/14) have been optimally designed in FEA and evaluated for geared MS wind generator drives using rare-earth-free materials, viz., ferrite PMs and WF coils. To escalate their potentials for industrial-scale applications, the study was implemented at small-scale (10 kW) as well as at large-scale (3 MW) power levels. From the MDO results, it was found that the ferrite PM–FSM performs better in terms of lowest torque ripple and active mass for both machine configurations at 10 kW power, whereas at 3 MW power, the WF–FSMs have better torque densities, while the ferrite PM–FSMs have better torque ripple values. Overall, the

minimization of the total active mass are better propagated in the 12/10 and 12/14 WF–FSMs compared to the ferrite PM–FSMs at 3 MW power due to inherent tradeoff uncovered in their aspect ratios and armature current densities. Consequently, to ensure the feasibility of the optimal design, it becomes necessary for the designer to appropriately set the margins of the aspect and split ratios before engaging them in such MDO procedure.

Based on some optimal benchmarks and irrespective of the power level, the 12/14 rare-earth-free machines were observed to be cheaper compared to the 12/10 machines by at least 10%, with the latter exhibiting higher inductance ratios. By further comparing the rare-earth-free benchmarks with rare-earth PM–FSMs, as well as two other classical MS wind generators (DFIG and PMSG), it was found, among other things, that, as the power level shifts from 10 kW to 3 MW, an improvement in terms of increased torque densities and reduced torque ripple values is obtained for the understudied machines. But, it was equally observed that the rare-earth-free designs do not exhibit better torque ripple values compared to rare-earth PM–FSMs as normally anticipated based on the flux focusing capabilities of FSMs. Additionally, at 3 MW, the benchmark comparisons revealed that the WF–FSM has the cheapest active material cost while the ferrite PM–FSM has the highest efficiency, but with significant underestimation of the copper resistance in the latter.

Thus, due to the interesting behavior observed for the WF–FSM at 3 MW, a 10 kW optimal design variant is benchmarked, manufactured, and tested for the first time, with some novel improvising, to serve as experimental validation for the study. The reported on-load measured results exhibited good confidence in tandem with a cocktail of FEA predictions.

APPENDIX

A. Evaluation of Electrical Frequency

The flux switching (alternating magnetic field) characteristics of FSMs within the same stator pole enable them to accomplish full electrical cycle in one rotor pitch. Hence, the electrical frequency, unlike in classical electrical machines, is given as

$$f_e = \frac{n_r N_r}{60} \tag{4}$$

where N_r is the rotor pole number and n_r is as previously defined. Thus, under the same speed operation as indicated in Table III, the electrical frequency of the 12/10 and 12/14 machines is 60 Hz and 84 Hz, respectively.

B. Measurements of Some Parameters

The core loss measurement is given as

$$P_{\text{core}} = \omega_e \tau_{\text{mech}} - P_{\text{out}} - P_{wf} - 3I_s^2 R_s \tag{5}$$

where ω_e is the electrical angular speed in rad/s, τ_{mech} is the input mechanical torque in N·m, P_{out} is the electrical output power in W, P_{wf} is the windage and frictional mechanical losses in W, R_s is the phase winding resistance in Ω, while I_s retains its former definition.

In order to institute uniformity with the efficiency calculated from FEA as adopted from [12] in this study, which is simply based on the total copper and core losses, the measured per unit efficiency is thus evaluated as

$$\eta = \frac{P_{\text{out}}}{P_{\text{out}} + 3I_s^2 R_s + I_F^2 R_F + P_{\text{core}}} \tag{6}$$

where I_F is the field current in A, R_F is the field resistance in Ω, and other parameters have their usual meaning.

Finally, the measured power factor and developed torque, which is the electromagnetic torque, are calculated as

$$pF = \frac{P_{\text{out}}}{3I_s V_s} \tag{7}$$

$$\tau_e = \frac{\omega_e \tau_{\text{mech}} - P_{\text{core}} - P_{wf}}{\omega_e} \tag{8}$$

where V_s is the rms phase voltage in V, and other parameters have their usual meaning.

ACKNOWLEDGMENT

The authors would like to thank K. Cloete and staff of the Electrical Machines Workshop, Stellenbosch University, for their assistance in the manufacturing and assembling of the generator prototype used in this study, as well as C. Botha for setting up the control drive used for the laboratory tests.

REFERENCES

[1] REN 21, Renewables 2017 Global Status Report (Paris: REN21 Secretariat), 2017. [Online]. Available: www.ren21.net/gsr

[2] J. H. J. Potgieter, "Optimal topology and critical evaluation of slip synchronous permanent magnet wind generator," *Ph.D. dissertation*, Dept. Elect. Electron. Eng., Stellenbosch Univ., Stellenbosch, South Africa, Apr. 2014.

[3] R.-J. Wang and S. Gerber, "Magnetically geared wind generator technologies: Opportunities and challenges," *Appl. Energy*, vol. 136, pp. 817–826, 2014.

[4] I. Boldea, L. Tutelea, and F. Blaabjerg, "High power wind generator designs with less or no PMs: An overview," in *Proc. 17th Int. Conf. Elect. Mach. Syst.*, Oct. 22–25, 2014, pp. 1–14.

[5] L. Shao *et al.*, "Influence of rotor-pole number on electromagnetic performance in 12-phase redundant switched flux permanent magnet machines for wind power generation," *IEEE Trans. Ind. Appl.*, vol. 53, no. 4, pp. 3305–3316, Jul./Aug. 2017.

[6] M. Cheng, W. Hua, J. Zhang, and W. Zhao, "Overview of stator–permanent magnet brushless machines," *IEEE Trans. Ind. Electron.*, vol. 58, no. 11, pp. 5087–5101, Nov. 2011.

[7] U. B. Akuru and M. J. Kamper, "Performance comparison of optimum wound–field and ferrite PM flux switching machines for wind energy applications," in *Proc. XXII Int. Conf. Elect. Mach.*, Lausanne, Switzerland, 2016, pp. 2478–2485.

[8] A. Fasolo, L. Alberti, and N. Bianchi, "Performance comparison between switching–flux and IPM machines with rare–earth and ferrite PMs," *IEEE Trans. Ind. Appl.*, vol. 50, no. 6, pp. 3708–3716, Nov./Dec. 2014.

[9] T. Raminosoa *et al.*, "Reduced rare–earth flux–switching machines for traction applications," *IEEE Trans. Ind. Appl.*, vol. 51, no. 4, pp. 2959–2971, Aug. 2015.

[10] L. Wang, S. Aleksandrov, Y. Tang, J. J. H. Paulides, and E. A. Lomonova, "Fault-tolerant electric drive and space-phasor modulation of flux-switching permanent magnet machine for aerospace application," *IET Elect. Power Appl.*, vol. 11, no. 8, pp. 1416–1423, Sep. 2017.

[11] Y. Tang, J. J. H. Paulides, T. E. Motoasca, and E. A. Lomonova, "Flux–switching machine with DC excitation," *IEEE Trans. Magn.*, vol. 48, no. 11, pp. 3583–3586, Nov. 2012.

[12] U. B. Akuru and M. J. Kamper, "Formulation and multi–objective design optimisation of wound–field flux switching machines for wind energy drives," *IEEE Trans. Ind. Electron.*, vol. 65, no. 2, pp. 1828–1836, Feb. 2018.

[13] N. Fernando, I. U. Nutkani, S. Saha, and M. Niakinezhad, "Flux switching machines: A review on design and applications," in *Proc. 20th Int. Conf. Elect. Mach. Syst.*, Sydney, NSW, Australia, 2017, pp. 1–6.
[14] W. Cao, Y. Xie, and Z. Tan, *Wind Turbine Generator Technologies.* London, U.K.: InTech, 2012.
[15] Y. Duan and D. M. Ionel, "A review of recent developments in electrical machine design optimization methods with a permanent–magnet synchronous motor benchmark study," *IEEE Trans. Ind. Appl.*, vol. 49, no. 3, pp. 1268–1275, May/Jun. 2013.
[16] K. Deb, A. Pratap, S. Agarwal, and T. Meyarivan, "A fast and elitist multiobjective genetic algorithm: NSGA–II," *IEEE Trans. Evol. Comput.*, vol. 6, no. 2, pp. 182–197, Apr. 2002.
[17] X. Wang, T. D. Strous, D. Lahaye, H. Polinder, and J. A. Ferreira, "Modeling and optimization of brushless doubly–fed induction machines using computationally efficient finite–element analysis," *IEEE Trans. Ind. Appl.*, vol. 52, no. 6, pp. 4525–4534, Nov./Dec. 2016.
[18] VisualDOC User's Manual: Version 8.0, Vanderplaats Research & Development, Inc., Colorado Springs, CO, USA, Feb. 2017.
[19] SEMFEM documentation. [Online]. Available: www0.sun.ac.za/semfem/index.html, Accessed on Jun. 27, 2018.
[20] U. B. Akuru, "Design optimisation and performance evaluation of flux switching machines for geared medium–speed wind generator drives," Ph.D. dissertation, Elect. Electron. Eng., Stellenbosch Univ., Stellenbosch, South Africa, Dec. 2017.
[21] H. Polinder, F. F. A. van der Pijl, G. J. de Vilder, and P. J. Tavner, "Comparison of direct–drive and geared generator concepts for wind turbines," *IEEE Trans. Energy Convers.*, vol. 21, no. 3, pp. 725–733, Sep. 2006.
[22] X. Zhu, W. Hua, Z. Wu, W. Huang, H. Zhang, and M. Cheng, "Analytical approach for cogging torque reduction in flux–switching permanent magnet machines based on magneto motive force–permeance model," *IEEE Trans. Ind. Electron.*, vol. 65, no. 3, pp. 1965–1979, Mar. 2018.

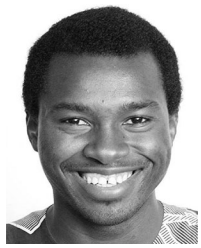

Udochukwu B. Akuru (M'13) was born in Lagos, Nigeria, on June 6, 1983. He received the B.Eng. and M.Eng. degrees from the University of Nigeria, Nsukka, Nigeria, in June 2013 and August 2008, respectively, and the Ph.D. degree in electrical engineering from Stellenbosch University, Stellenbosch, South Africa, in December 2017.

He is a Lecturer at the University of Nigeria, but is currently on leave to Stellenbosch University, as a Postdoctoral Research Fellow. He has a number of peer-reviewed journal and conference papers. His main research interests include electrical drives and renewable energy technologies with competency in finite element analyses of electrical machines.

Dr. Akuru is a registered member of the Council for the regulation of Engineering in Nigeria (COREN), volunteer to IEEE associated societies, committees, and groups such as IEEE IAS EMC and IEEE IES EMTC. He acts as a Reviewer to major IEEE conferences and transactions.

Maarten J. Kamper (SM'08) received the M.Sc. (Eng.) and Ph.D. degrees from the University of Stellenbosch, Stellenbosch, South Africa, in 1987 and 1996, respectively.

Since 1989, he has been with the academic staff of the Department of Electrical and Electronic Engineering, University of Stellenbosch, where he is currently a Professor of electrical machines and drives. His research interests include computer-aided design and control of reluctance, permanent magnet, and inductance machine drives.

Prof. Kamper is a South African National Research Foundation Supported Scientist and a Registered Professional Engineer in South Africa.